

Ultrahigh Thermal Conductivity of Cubic Boron Arsenide with an Unexpectedly Strong Temperature Dependence

Songrui Hou^{1†}, Fengjiao Pan^{2†}, Xinpeng Shi³, Zahra Ebrahim Nataj⁴, Fariborz Kargar⁴, Alexander A. Balandin⁴, David G. Cahill⁵, Chen Li^{1,3*}, Zhifeng Ren^{2*}, Richard B. Wilson^{1,3*}

Affiliations:

¹Materials Science and Engineering, University of California, Riverside, CA, 92521, USA.

²Department of Physics and Texas Center for Superconductivity (TcSUH), University of Houston, Houston, TX 77204, USA.

³Department of Mechanical Engineering, University of California, Riverside, CA, 92521, USA.

⁴Department of Materials Science and Engineering, University of California, Los Angeles, California 90095, USA.

⁵Department of Materials Science and Engineering and Materials Research Laboratory, University of Illinois at Urbana-Champaign, Urbana, IL 61801, USA.

*Corresponding author. Email: chenli@ucr.edu (C.L.); zren@uh.edu (Z.R.); rwilson@ucr.edu (R.B.W.)

†These authors contributed equally to this work.

Abstract: Materials with high thermal conductivity are needed to conduct heat away from hot spots in power electronics and optoelectronic devices. Cubic boron arsenide (c-BAs) has a high thermal conductivity due to its special phonon dispersion relation. Previous experimental studies of c-BAs report a room-temperature thermal conductivity between 1000 and 1300 watts per meter-kelvin. We synthesized high purity c-BAs single crystals with room-temperature thermal conductivity of 1500 watts per meter-kelvin. We observed its thermal conductivity to be proportional to the inverse square of temperature between 300 and 600 kelvin, a stronger dependence than predicted by state-of-the-art theory.

One-Sentence Summary: High purity c-BAs crystals have a thermal conductivity of 1500 W m⁻¹ K⁻¹ and a temperature dependence of 1/T² between 300 and 600 K.

Main Text:

Cubic boron arsenide (c-BAs, for simplicity, BAs is used throughout the paper) is of interest for next generation electronics due to its combined high thermal conductivity ($> 1000 \text{ W m}^{-1} \text{ K}^{-1}$) and high carrier mobility ($> 1400 \text{ cm}^2 \text{ V}^{-1} \text{ s}^{-1}$) (1–8). BAs's exceptional transport properties were first predicted by first-principles calculations that considered the effect of its special phonon dispersion on phonon scattering (3, 6, 7, 9). The difference in atomic mass between B and As leads to a large acoustic-optical (*a-o*) phonon frequency gap. This large gap, together with bunching of acoustic phonon branches and unusual chemical bonding (9) leads to weak phonon-phonon scattering. Weak polarity and high frequency of optical phonons suppress polar scattering of charge carriers (10). As a result, both heat carriers (acoustic phonons) and charge carriers (electrons and holes) have long mean free paths.

First-principles calculations predict a room-temperature thermal conductivity of $\approx 1200 \text{ W m}^{-1} \text{ K}^{-1}$ for $^{\text{nat}}$ BAs (3, 11, 12), and $\approx 1380 \text{ W m}^{-1} \text{ K}^{-1}$ for isotopically pure BAs (13). These predictions are in reasonable agreement with prior experimental observations of Λ between 1000 and 1300 $\text{W m}^{-1} \text{ K}^{-1}$ for natural BAs (4, 5), and between 1160 and 1260 $\text{W m}^{-1} \text{ K}^{-1}$ for isotopically enriched BAs (3, 13, 14). (Early theoretical calculations predicted higher values of ≈ 1400 and $1700 \text{ W m}^{-1} \text{ K}^{-1}$ for natural and isotopically pure BAs, respectively (7, 15). Subsequent improvements in computational approach led to a $\approx 20\%$ reduction in predictions for Λ (3, 11–13).)

Theoretical predictions for the intrinsic Λ of BAs assume minimal defects. Recent studies suggest defect levels in BAs crystals studied to date are not negligible. Chen *et al.* used secondary ion mass spectroscopy and electron probe microanalysis to study impurities in BAs crystals (16). The crystals were prepared in the same way as those studied in Ref. (3) and possessed room-temperature $\Lambda \approx 900 \text{ W m}^{-1} \text{ K}^{-1}$. They observed a Si impurity level of 0.047 at% ($3.4 \times 10^{19} \text{ cm}^{-3}$). BAs crystals are often reported to have peaks in their photoluminescence spectra near 1.5 eV (17, 18). Originally, these peaks were interpreted to imply a band gap of 1.5 eV in BAs (19, 20). However, recent studies have found the band gap of BAs to be between 1.8 and 2 eV (17, 18, 21–23), and credit photoluminescence peaks at 1.5 eV to group IV impurities (18).

Temperature-dependent thermal conductivity (Λ vs. T) measurements can help identify the impact of defects on thermal transport. In insulating materials, Λ vs. T hinges on the temperature (T) dependence of phonon scattering rates. Phonon-defect scattering rates are independent of T (24, 25), while phonon-phonon scattering rates are temperature sensitive (7). So, Λ is expected to vary less with temperature if defect concentrations are appreciable. Reports for Λ vs. T between 300 and 600 K in BAs vary between $\Lambda \propto 1/T^{1.3}$ and $1/T^2$ (3–5). First-principles calculations predict $\Lambda \propto 1/T^{1.6}$ between 300 and 600 K for $^{\text{nat}}$ BAs (3, 7). For isotopically pure BAs, its temperature dependence is predicted to fall between $\Lambda \propto 1/T^{1.7}$ and $1/T^{1.8}$ (9, 13, 15). Samples with higher defect concentrations are expected to have lower ambient thermal conductivity and weaker temperature dependence due to phonon-defect scattering. However, prior experimental results on BAs from different groups do not follow this trend (3–5). Kang *et al.* report a room-temperature thermal conductivity of $1300 \text{ W m}^{-1} \text{ K}^{-1}$ with a $\Lambda \propto 1/T^{1.3}$ dependence (4), while Tian *et al.* report a lower ambient thermal conductivity of $1160 \text{ W m}^{-1} \text{ K}^{-1}$ with $\Lambda \propto 1/T^2$ (3).

To study the temperature dependent thermal conductivity of BAs, we synthesized a variety of BAs crystals by chemical vapor transport (3, 26). All source ingredients involved in the synthesis

process were purchased from Alfa Aesar with high purity (metal basis). To synthesize BAs crystals, source boron (B, 99.9999%), arsenic (As, 99.99999%), and transport agent iodine (I₂, 99.9985%) were sealed in a fused quartz tube under vacuum (10^{-4} Torr). The boron source was isotopically enriched ^{11}B to an isotope purity $\geq 98\%$. A piece of quartz fiber or GaAs wafer was fixed on the other end of the tube as nucleation sites for crystal growth. Then the sealed quartz tube was placed into a two-zone horizontal tube furnace for crystal growth, with high temperature for source side and low temperature for growth side. The high-temperature zone of the furnace was heated up to 1168 K while the low-temperature zone was heated up to 1063 K. After crystal growth, the furnace was cooled down naturally to room temperature.

We characterized our BAs samples using X-ray diffraction (XRD), Raman scattering, photoluminescence (PL), and Brillouin scattering (Figs. S1-S4). The XRD results were consistent with a (111) growth facet. We observed consistent Raman peaks as prior observations on BAs with similar isotope concentrations (13, 27). In most samples, we observed PL spectra centered near 1.75 eV. But some samples exhibited additional PL peaks centered at lower energies. Our PL results were consistent with the spectra observed in prior studies (1, 2, 17, 18).

We conducted Brillouin-Mandelstam spectroscopy (28) on nine BAs samples, a technique used to measure low-frequency acoustic phonons. A 532 nm laser beam was shined on the BAs sample at an incident angle of 30 degrees. We measured the backscattered light that was inelastically scattered by acoustic phonon modes. We observed three peaks in the Brillouin spectra associated with two transverse acoustic (TA) and one longitudinal acoustic (LA) phonons at 58.8, 62.1, and 101.6 GHz, respectively. These frequencies correspond to TA and LA sound velocities of 4800, 5080, and 8320 m/s along the direction of the refracted laser beam, which is $\sim 8^\circ$ from the [111] direction. Our Brillouin scattering results are consistent with prior experimental results (29) of 4978 and 8513 m/s for the transverse and longitudinal acoustic phonons along [111] direction, respectively, obtained using picosecond interferometry.

Time-domain thermoreflectance (TDTR) measurements reveal the ambient thermal conductivity ($\Lambda_{300\text{K}}$) of synthesized crystals are as high as $1500 \text{ W m}^{-1} \text{ K}^{-1}$ (sample BAs-1500), higher than previous experimental observations (3–5). As part of this study, we measured the thermal conductivity of more than fifty BAs crystals. Among these, four crystals had thermal conductivity above $1400 \text{ W m}^{-1} \text{ K}^{-1}$. TDTR data for one of the high-thermal-conductivity crystals is shown in Fig. 1A. TDTR data for the other three are shown in Fig. S5. In TDTR experiments, the $-V_{in}/V_{out}$ signal describes the thermal response of the sample to optical heating. We fit the TDTR signals with a heat diffusion model to extract the thermal conductivity of BAs (30). The temperature-dependent parameters in the heat diffusion model are shown in Fig. S6.

We observe that BAs crystals with $\Lambda_{300\text{K}} = 1500 \text{ W m}^{-1} \text{ K}^{-1}$ exhibit $\Lambda \propto 1/T^2$ between 300 and 600 K (Fig. 1B). This is a stronger temperature dependence than being predicted by first-principles calculations (3, 7, 9, 13, 15), and stronger than prior experimental results of BAs (4, 5). We corroborated the observed $1/T^2$ dependence by performing separate beam-offset TDTR measurements (31) of the in-plane thermal conductivity versus temperature on the sample in Fig. 1. Additionally, we measured another BAs sample with $\Lambda_{300\text{K}} = 1500 \text{ W m}^{-1} \text{ K}^{-1}$ and observed the same temperature dependence, see Fig. S9. Details about our TDTR and beam offset measurements can be found in the Supplementary Materials (Figs. S6 – S13).

To investigate the mean-free-path distribution of heat-carrying phonons in BAs, we conducted TDTR measurements as a function of laser spot size (32–34). When the laser spot size is small,

the in-plane heat current carried by phonons with long mean free path is less than what Fourier’s law predicts (32). This results in spot-size dependent apparent thermal conductivity (Λ_A), where we define Λ_A as the Λ that yields the best fit of the heat diffusion model to the experimental data. We measured Λ_A of the BAs-1500 sample at temperatures of 300, 450, and 600 K (Fig. 1C). At 300 K, a spot-size reduction from 15 to 1.7 μm led to a $\sim 20\%$ reduction in Λ_A . A similar suppression of Λ_A was observed in silicon and diamond (32–34). The 20% drop we observed is much smaller than prior reports for Λ_A versus spot size in BAs (4, 5). A weak dependence of Λ_A on spot size for BAs is in qualitative agreement with first-principles calculations (3), and consistent with Peierls-Boltzmann transport equation simulations of non-diffusive heat transfer in TDTR measurements of BAs (35). First-principles calculations predict 80% of the heat is carried by phonons with mean free paths between 0.3 and 1.5 μm . At 450 and 600 K, laser spot size does not affect Λ_A . This suggests that for $T \geq 450$ K, the mean free paths of all heat-carrying phonons are less than 1.7 μm . To avoid mean-free-path effects in the rest of our experiments, we used a $1/e^2$ laser radius greater than 10 μm .

To further explore the temperature-dependent thermal conductivity of BAs, we selected four other BAs samples and measured their Λ vs. T . These samples had $\Lambda_{300\text{K}}$ of 1350, 1200, 1000, and 700 $\text{W m}^{-1} \text{K}^{-1}$. We also measured a type IIa diamond crystal from Element Six as a control sample. We fit the measured data of Λ vs. T by $\Lambda \propto 1/T^\alpha$ to obtain the temperature exponent α . We plot α vs. $\Lambda_{300\text{K}}$ for the selected BAs samples (Fig. 2B). The temperature exponent of diamond is 1.2, in good agreement with prior reports (4, 7). As $\Lambda_{300\text{K}}$ decreases, the temperature dependence weakens. As described above, this is expected. Phonon-defect scattering rates are proportional to the concentration of defects. The higher the defect concentration, the lower the ambient thermal conductivity. Since defect concentrations are independent of temperature, phonon-defect scattering lowers α .

The temperature dependence of Λ we observe for BAs is unusually large. At high temperatures, the temperature dependence of Λ is primarily determined by the type of scattering processes that limit mean free paths of heat carrying phonons. In most high purity single crystals, three-phonon scattering is the dominant process, resulting in $\Lambda \propto 1/T$ ($\alpha = 1$) (7, 9). A higher temperature exponent can indicate higher-order phonon scattering processes (9). Three-phonon-scattering rates increase linearly with temperature, while four-phonon-scattering rates increase quadratically with temperature (7).

In the limit where four-phonon scattering processes dominate, α is expected to be close to but smaller than 2 in defect-free samples (7). Some materials exhibit $\alpha > 1$, but it is rare for α being close to 2. For instance, BP and InP have temperature exponents of 1.4 (36) and 1.5 (37), respectively. BP and InP are III-V semiconductors with an *a-o* gap due to the large mass ratio between constituent atoms (6, 9). A large *a-o* gap limits the phase space of three-phonon scattering, which can increase the importance of four-phonon scattering processes. BP, InP, and BAs are examples of this trend. The relationship between α and mass ratio for III-V compounds with zincblende structure is summarized in Fig. S14.

In BAs, four-phonon-scattering processes are expected to be important, but not dominant (7, 9, 15). For $^{\text{nat}}$ BAs, theory predicts $\alpha \approx 1.6$ (3, 7). For isotopically pure BAs, theoretical predictions for α lie between 1.7 and 1.8 (9, 13, 15). The small disagreement between theory and experiment for α could originate from several factors. The ratio of four-phonon to three-phonon scattering rates in BAs could be higher than predictions (9, 13, 15). Although first-principles calculations do not use fitting parameters, their accuracy is affected by a variety of factors (11, 38). Jain and

McGaughey found that the choice of exchange-correlation function can change the predicted thermal conductivity of Si by $\sim 30\%$ (38). Zhou *et al.* report that fourth-order force constants are sensitive to the energy surface roughness of the exchange correlation functionals (11).

Another possible explanation for why α in BAs is higher than theoretical predictions is temperature-induced changes of the phonon dispersion. Three- and four-phonon scattering rates in BAs are sensitive to the a - o gap and the bunching of acoustic modes (6, 39–41). To investigate this hypothesis, we conducted temperature-dependent Brillouin and Raman scattering experiments to assess how phonon frequencies evolve with increasing temperature, see Fig. S15 and S16. Our Brillouin scattering measurements revealed that the longitudinal acoustic phonon frequencies near the zone center change by less than 1% upon heating from 300 to 600 K. Raman scattering measurements indicated that the optical phonon frequency at zone center experiences a 1% decrease. Therefore, it is unlikely that temperature-induced changes to the phonon dispersion can explain why Λ is proportional to $1/T^2$. We note that neither Raman nor Brillouin scattering measures the high-frequency acoustic phonons that are most responsible for heat transfer in BAs. So, our experiments do not definitively exclude temperature-induced changes in phonon dispersion as an important effect.

To characterize defects in our samples, we performed pump/probe transient reflectivity microscopy (TRM) on bare BAs samples with incident photon energy of 1.58 eV (Fig. 3). In these experiments, we irradiated the BAs surface with a pump beam. We measured the intensity of a reflected probe beam as a function of pump/probe delay time. The laser energy is ~ 0.26 eV less than the 1.84 eV band gap of BAs (17, 23). Therefore, in the absence of impurities, we expect negligible absorption and no pump-induced change in the reflectance of BAs. In the presence of impurities that form defect states in the band gap, we expect measurable TRM signal. The effect of an impurity on absorption will depend on the energy level of the defect state. If the defect state's energy is near the conduction or valence band edges (ionization energy $\leq 3k_B T \approx 75$ meV), the impurity affects absorption by introducing free carriers, see Fig. 3A. Alternatively, defects that form states far from the conduction or valence band edges will allow optical transitions to (or from) the defect state, see Fig. 3B. For impurities with moderate ionization energies, *e.g.*, 100 - 300 meV, we expect both these absorption mechanisms will matter.

We observed non-zero TRM signals in most BAs samples, including the ones with $\Lambda_{300\text{K}} = 1500 \text{ W m}^{-1} \text{ K}^{-1}$ (Fig. 3C). We performed TRM measurements at ≥ 10 spots on each sample. Most measurements were performed with a pump fluence of 0.7 J/m^2 and probe power of 2 mW. A few measurements were conducted with different pump fluences and probe powers. For these measurements, to facilitate comparisons in Fig. 3, we scaled the signals by a factor to account for the difference in pump fluence. Each marker in Fig. 3C and 3F represents the average value of all measured spots, while error bars represent the standard deviation. The data in Fig. 3D and 3E are for individual spots, not averages. We observed a correlation between $\Lambda_{300\text{K}}$ and TRM signals (Fig. 3C). We performed wavelength-dependent pump/probe TRM measurements (Fig. 3E) on BAs-1500 as well as two BAs samples whose $\Lambda_{300\text{K}}$ are 1000 (BAs-1000) and $400 \text{ W m}^{-1} \text{ K}^{-1}$ (BAs-400), respectively. For these measurements, we fixed our laser beam on a region that had a small TRM signal, *i.e.*, a region with a low density of defects. We observed an increasing TRM signal as photon energy approaches the band gap of BAs. As a set of control experiments, we also performed TRM measurements with a laser energy of 1.58 eV on crystals with different band gaps: Si (1.12 eV) (42), GaAs (1.42 eV) (43), GaP (2.26 eV) (44), and GaN (3.39 eV) (45).

The carrier densities of the GaP and GaN samples are $(4\sim 6) \times 10^{16} \text{ cm}^{-3}$ and $\sim 1 \times 10^{18} \text{ cm}^{-3}$, respectively. As expected, TRM signals are large for crystals with band gaps less than 1.58 eV, and negligibly small for crystals with band gaps greater than 1.58 eV, see Fig. 3F. We also measured intentionally doped n-type and p-type GaP crystals with specified carrier concentrations on the order of 10^{18} cm^{-3} . The TRM signal from BAs-1500 is the same order of magnitude as the TRM signal from GaP with $\approx 10^{18} \text{ cm}^{-3}$ p-type Zn impurities, see Fig. S17. Further details related to our TRM measurements can be found in the Supplementary text.

Based on the TRM results, BAs samples with $\Lambda_{300\text{K}}$ of $1500 \text{ W m}^{-1} \text{ K}^{-1}$ are not defect-free. This indicates that the intrinsic thermal conductivity may be larger than $1500 \text{ W m}^{-1} \text{ K}^{-1}$, and the intrinsic temperature dependence between 300 and 600 K of BAs may be stronger than $1/T^2$. Existing first-principles calculations cannot explain the coexistence of $\Lambda_{300\text{K}} > 1500 \text{ W m}^{-1} \text{ K}^{-1}$ and $\alpha \geq 2$. First principles calculations predict $\Lambda_{300\text{K}}$ of $3100 \text{ W m}^{-1} \text{ K}^{-1}$ and $\alpha = 0.9$ if only considering three-phonon scattering (13). In the limit that four-phonon scattering is the only dominant scattering process, $\Lambda_{300\text{K}}$ is expected to be $\approx 15000 \text{ W m}^{-1} \text{ K}^{-1}$ (not a typo, see Supplementary Figure 10 in Ref. (39)) with $\alpha = 2$ (7, 39). As noted above, one possible explanation for $\alpha \geq 2$ is that higher-order processes than four-phonon scattering affect Λ in BAs. While adding higher-order processes to existing first-principles calculations would increase α , it would also lower predictions for $\Lambda_{300\text{K}}$. Therefore, the current ultrahigh thermal conductivity at room temperature and its strong T dependence ($\alpha = 2$) motivates further theoretical work to understand these unexpected observations. Moreover, it points to even higher thermal conductivity values potentially being achievable with improved BAs synthesis, with corresponding increased opportunities for applications.

References

1. S. Yue, F. Tian, X. Sui, M. Mohebinia, X. Wu, T. Tong, Z. Wang, B. Wu, Q. Zhang, Z. Ren, J. Bao, X. Liu, High ambipolar mobility in cubic boron arsenide revealed by transient reflectivity microscopy. *Science* **377**, 433–436 (2022).
2. J. Shin, G. A. Gamage, Z. Ding, K. Chen, F. Tian, X. Qian, J. Zhou, H. Lee, J. Zhou, L. Shi, T. Nguyen, F. Han, M. Li, D. Broido, A. Schmidt, Z. Ren, G. Chen, High ambipolar mobility in cubic boron arsenide. *Science* **377**, 437–440 (2022).
3. F. Tian, B. Song, X. Chen, N. K. Ravichandran, Y. Lv, K. Chen, S. Sullivan, J. Kim, Y. Zhou, T.-H. Liu, M. Goni, Z. Ding, J. Sun, G. A. G. Udalamatta Gamage, H. Sun, H. Ziyae, S. Huyan, L. Deng, J. Zhou, A. J. Schmidt, S. Chen, C.-W. Chu, P. Y. Huang, D. Broido, L. Shi, G. Chen, Z. Ren, Unusual high thermal conductivity in boron arsenide bulk crystals. *Science* **361**, 582–585 (2018).
4. J. S. Kang, M. Li, H. Wu, H. Nguyen, Y. Hu, Experimental observation of high thermal conductivity in boron arsenide. *Science* **361**, 575–578 (2018).
5. S. Li, Q. Zheng, Y. Lv, X. Liu, X. Wang, P. Y. Huang, D. G. Cahill, B. Lv, High thermal conductivity in cubic boron arsenide crystals. *Science* **361**, 579–581 (2018).

6. L. Lindsay, D. A. Broido, T. L. Reinecke, First-Principles Determination of Ultrahigh Thermal Conductivity of Boron Arsenide: A Competitor for Diamond? *Phys. Rev. Lett.* **111**, 025901 (2013).
7. T. Feng, L. Lindsay, X. Ruan, Four-phonon scattering significantly reduces intrinsic thermal conductivity of solids. *Phys. Rev. B* **96**, 161201 (2017).
8. E. Guzman, F. Kargar, A. Patel, S. Vishwakarma, D. Wright, R. B. Wilson, D. J. Smith, R. J. Nemanich, A. A. Balandin, Optical and acoustic phonons in turbostratic and cubic boron nitride thin films on diamond substrates. *Diamond and Related Materials* **140**, 110452 (2023).
9. N. K. Ravichandran, D. Broido, Phonon-Phonon Interactions in Strongly Bonded Solids: Selection Rules and Higher-Order Processes. *Phys. Rev. X* **10**, 021063 (2020).
10. T.-H. Liu, B. Song, L. Meroueh, Z. Ding, Q. Song, J. Zhou, M. Li, G. Chen, Simultaneously high electron and hole mobilities in cubic boron-V compounds: BP, BAs, and BSb. *Phys. Rev. B* **98**, 081203 (2018).
11. H. Zhou, S. Zhou, Z. Hua, K. Bawane, T. Feng, Extreme sensitivity of higher-order interatomic force constants and thermal conductivity to the energy surface roughness of exchange-correlation functionals. *Applied Physics Letters* **123**, 192201 (2023).
12. Z. Han, X. Yang, W. Li, T. Feng, X. Ruan, FourPhonon: An extension module to ShengBTE for computing four-phonon scattering rates and thermal conductivity. *Computer Physics Communications* **270**, 108179 (2022).
13. K. Chen, B. Song, N. K. Ravichandran, Q. Zheng, X. Chen, H. Lee, H. Sun, S. Li, G. A. G. Udalamatta Gamage, F. Tian, Z. Ding, Q. Song, A. Rai, H. Wu, P. Koirala, A. J. Schmidt, K. Watanabe, B. Lv, Z. Ren, L. Shi, D. G. Cahill, T. Taniguchi, D. Broido, G. Chen, Ultrahigh thermal conductivity in isotope-enriched cubic boron nitride. *Science* **367**, 555–559 (2020).
14. H. Sun, K. Chen, G. A. Gamage, H. Ziyae, F. Wang, Y. Wang, V. G. Hadjiev, F. Tian, G. Chen, Z. Ren, Boron isotope effect on the thermal conductivity of boron arsenide single crystals. *Materials Today Physics* **11**, 100169 (2019).
15. X. Yang, T. Feng, J. Li, X. Ruan, Stronger role of four-phonon scattering than three-phonon scattering in thermal conductivity of III-V semiconductors at room temperature. *Phys. Rev. B* **100**, 245203 (2019).
16. X. Chen, C. Li, Y. Xu, A. Dolocan, G. Seward, A. Van Roekeghem, F. Tian, J. Xing, S. Guo, N. Ni, Z. Ren, J. Zhou, N. Mingo, D. Broido, L. Shi, Effects of Impurities on the Thermal and Electrical Transport Properties of Cubic Boron Arsenide. *Chem. Mater.* **33**, 6974–6982 (2021).
17. S. Yue, G. A. Gamage, M. Mohebinia, D. Mayerich, V. Talari, Y. Deng, F. Tian, S.-Y. Dai, H. Sun, V. G. Hadjiev, W. Zhang, G. Feng, J. Hu, D. Liu, Z. Wang, Z. Ren, J. Bao,

- Photoluminescence mapping and time-domain thermo-photoluminescence for rapid imaging and measurement of thermal conductivity of boron arsenide. *Materials Today Physics* **13**, 100194 (2020).
18. J. L. Lyons, J. B. Varley, E. R. Glaser, J. A. Freitas, J. C. Culbertson, F. Tian, G. A. Gamage, H. Sun, H. Ziyace, Z. Ren, Impurity-derived *p*-type conductivity in cubic boron arsenide. *Applied Physics Letters* **113**, 251902 (2018).
 19. I. H. Nwigboji, Y. Malozovsky, L. Franklin, D. Bagayoko, Calculated electronic, transport, and related properties of zinc blende boron arsenide (zb-BAs). *Journal of Applied Physics* **120**, 145701 (2016).
 20. S. Wang, S. F. Swingle, H. Ye, F.-R. F. Fan, A. H. Cowley, A. J. Bard, Synthesis and Characterization of a *p*-Type Boron Arsenide Photoelectrode. *J. Am. Chem. Soc.* **134**, 11056–11059 (2012).
 21. K. Bushick, K. Mengle, N. Sanders, E. Kioupakis, Band structure and carrier effective masses of boron arsenide: Effects of quasiparticle and spin-orbit coupling corrections. *Applied Physics Letters* **114**, 022101 (2019).
 22. S. Chae, K. Mengle, J. T. Heron, E. Kioupakis, Point defects and dopants of boron arsenide from first-principles calculations: Donor compensation and doping asymmetry. *Applied Physics Letters* **113**, 212101 (2018).
 23. H. Zhong, F. Pan, S. Yue, C. Qin, V. Hadjiev, F. Tian, X. Liu, F. Lin, Z. Wang, J. Bao, Idealizing Tauc Plot for Accurate Bandgap Determination of Semiconductor with Ultraviolet–Visible Spectroscopy: A Case Study for Cubic Boron Arsenide. *J. Phys. Chem. Lett.*, 6702–6708 (2023).
 24. B. Abeles, Lattice Thermal Conductivity of Disordered Semiconductor Alloys at High Temperatures. *Phys. Rev.* **131**, 1906–1911 (1963).
 25. P. G. Klemens, Thermal Resistance due to Point Defects at High Temperatures. *Phys. Rev.* **119**, 507–509 (1960).
 26. F. Tian, B. Song, B. Lv, J. Sun, S. Huyan, Q. Wu, J. Mao, Y. Ni, Z. Ding, S. Huberman, T.-H. Liu, G. Chen, S. Chen, C.-W. Chu, Z. Ren, Seeded growth of boron arsenide single crystals with high thermal conductivity. *Appl. Phys. Lett.* **112**, 031903 (2018).
 27. A. Rai, S. Li, H. Wu, B. Lv, D. G. Cahill, Effect of isotope disorder on the Raman spectra of cubic boron arsenide. *Phys. Rev. Materials* **5**, 013603 (2021).
 28. F. Kargar, A. A. Balandin, Advances in Brillouin–Mandelstam light-scattering spectroscopy. *Nat. Photon.* **15**, 720–731 (2021).
 29. S. Mahat, S. Li, H. Wu, P. Koirala, B. Lv, D. G. Cahill, Elastic constants of cubic boron phosphide and boron arsenide. *Phys. Rev. Materials* **5**, 033606 (2021).

30. D. G. Cahill, Analysis of heat flow in layered structures for time-domain thermoreflectance. *Review of Scientific Instruments* **75**, 5119–5122 (2004).
31. J. P. Feser, J. Liu, D. G. Cahill, Pump-probe measurements of the thermal conductivity tensor for materials lacking in-plane symmetry. *Review of Scientific Instruments* **85**, 104903 (2014).
32. R. B. Wilson, D. G. Cahill, Anisotropic failure of Fourier theory in time-domain thermoreflectance experiments. *Nat Commun* **5**, 5075 (2014).
33. A. J. Minnich, J. A. Johnson, A. J. Schmidt, K. Esfarjani, M. S. Dresselhaus, K. A. Nelson, G. Chen, Thermal Conductivity Spectroscopy Technique to Measure Phonon Mean Free Paths. *Phys. Rev. Lett.* **107**, 095901 (2011).
34. R. B. Wilson, D. G. Cahill, Limits to Fourier theory in high thermal conductivity single crystals. *Applied Physics Letters* **107**, 203112 (2015).
35. C. Hua, L. Lindsay, X. Chen, A. J. Minnich, Generalized Fourier's law for nondiffusive thermal transport: Theory and experiment. *Phys. Rev. B* **100**, 085203 (2019).
36. Q. Zheng, S. Li, C. Li, Y. Lv, X. Liu, P. Y. Huang, D. A. Broido, B. Lv, D. G. Cahill, High Thermal Conductivity in Isotopically Enriched Cubic Boron Phosphide. *Adv. Funct. Mater.* **28**, 1805116 (2018).
37. I. Kudman, E. F. Steigmeier, Thermal Conductivity and Seebeck Coefficient of InP. *Phys. Rev.* **133**, A1665–A1667 (1964).
38. A. Jain, A. J. H. McGaughey, Effect of exchange–correlation on first-principles-driven lattice thermal conductivity predictions of crystalline silicon. *Computational Materials Science* **110**, 115–120 (2015).
39. N. K. Ravichandran, D. Broido, Non-monotonic pressure dependence of the thermal conductivity of boron arsenide. *Nat Commun* **10**, 827 (2019).
40. S. Hou, B. Sun, F. Tian, Q. Cai, Y. Xu, S. Wang, X. Chen, Z. Ren, C. Li, R. B. Wilson, Thermal Conductivity of BAs under Pressure. *Adv Elect Materials*, 2200017 (2022).
41. S. Li, Z. Qin, H. Wu, M. Li, M. Kunz, A. Alatas, A. Kavner, Y. Hu, Anomalous thermal transport under high pressure in boron arsenide. *Nature* **612**, 459–464 (2022).
42. W. Bludau, A. Onton, W. Heinke, Temperature dependence of the band gap of silicon. *Journal of Applied Physics* **45**, 1846–1848 (1974).
43. M. D. Sturge, Optical Absorption of Gallium Arsenide between 0.6 and 2.75 eV. *Phys. Rev.* **127**, 768–773 (1962).
44. M. R. Lorenz, G. D. Pettit, R. C. Taylor, Band Gap of Gallium Phosphide from 0 to 900°K and Light Emission from Diodes at High Temperatures. *Phys. Rev.* **171**, 876–881 (1968).

45. H. P. Maruska, J. J. Tietjen, THE PREPARATION AND PROPERTIES OF VAPOR-DEPOSITED SINGLE-CRYSTAL-LINE GaN. *Applied Physics Letters* **15**, 327–329 (1969).

Acknowledgments:

Funding:

ULTRA, an Energy Frontier Research Center funded by the U.S. Department of Energy (DOE), Office of Science, Basic Energy Sciences (BES), Award #DE-SC0021230 (RW)

National Science Foundation (NSF) Award #1750786 (CL)

National Science Foundation (NSF) *via* a Major Research Instrumentation (MRI) project DMR 2019056 (AAB and FK)

Author contributions:

Conceptualization: R.B.W., Z.R.

Resources: F.P. and Z.R. performed the crystal growth.

Investigation: S.H., R.B.W., and D.G.C. performed time-domain thermorefectance measurements. S.H. and R.B.W. performed beam offset measurements, transient reflectivity microscopy. S. H. performed Raman scattering, photoluminescence, and forced Brillouin scattering measurements. F.P. performed X-ray diffraction, X.S. performed atomic force microscopy. Z.E., F.K., and A.B. performed Brillouin-Mandelstam spectroscopy scattering.

Formal Analysis: S.H. and R.B.W. performed thermal modelling.

Visualization: S.H.

Funding acquisition: R.B.W., C.L., Z.R.

Project administration: R.B.W., C.L., Z.R.

Supervision: R.B.W., C.L., Z.R.

Writing – original draft: S.H., R.B.W.

Writing – review & editing: all authors

Competing interests: Authors declare that they have no competing interests.

Data and materials availability: All data are available in the main text or the supplementary materials.

Supplementary Materials

Materials and Methods

Supplementary Text

Figs. S1 to S19

Tables S1 to S2

References (46 – 77)

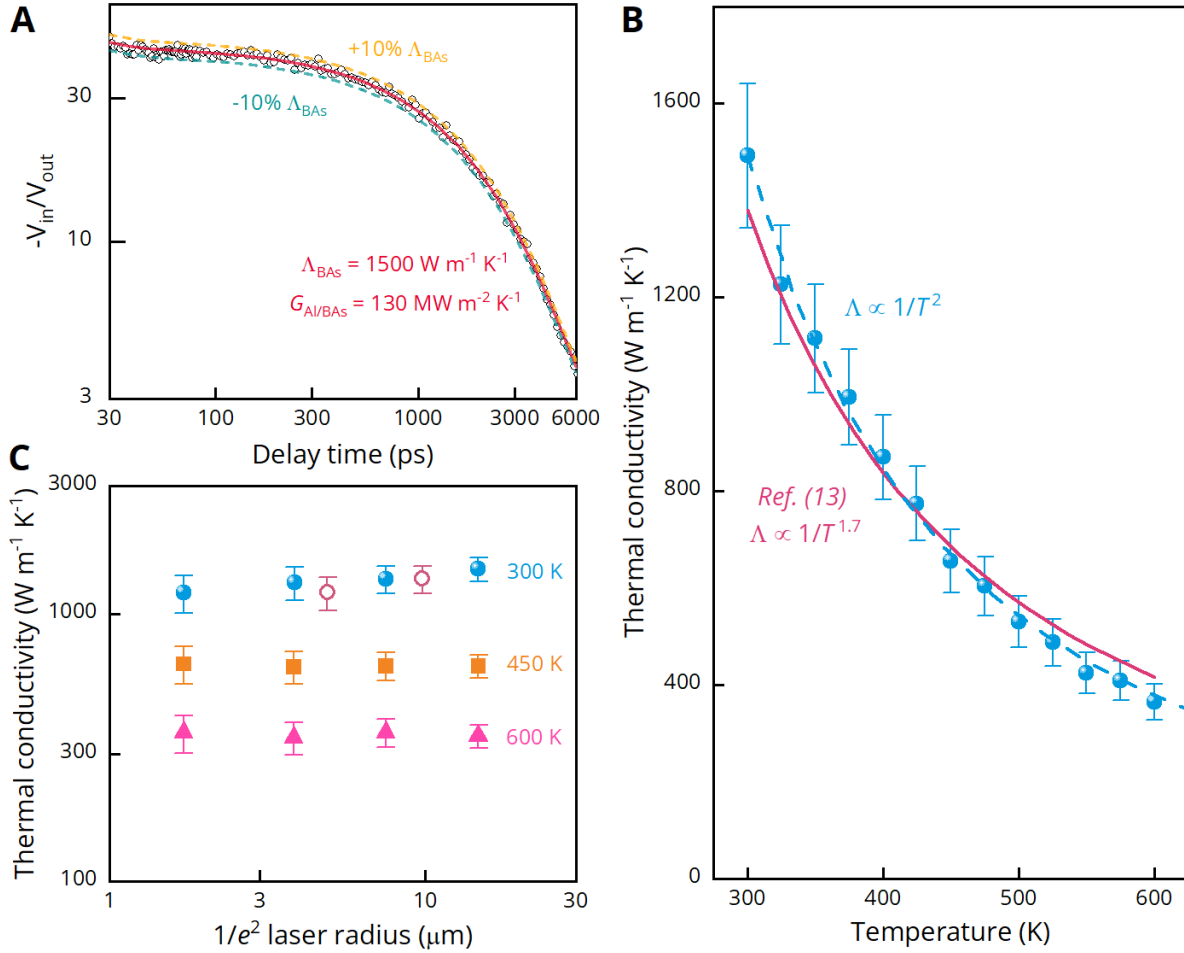


Fig. 1. Thermal conductivity of BAs. (A) Time domain thermoreflectance data with the best fit of thermal model (red line) for a high purity BAs crystal with $\Lambda \approx 1500 \text{ W m}^{-1} \text{ K}^{-1}$. The interface conductance between Al thin-film transducer and BAs crystal, which is also a fit parameter in the thermal model, is $130 \text{ MW m}^{-2} \text{ K}^{-1}$. The temperature-dependent interface conductance is shown in Fig. S6B. (B) BAs thermal conductivity versus temperature (markers), along with theoretical predictions for isotopically pure BAs (13). The blue dashed line is a $\Lambda \propto 1/T^2$ fit to our data. (C) Apparent thermal conductivity of BAs versus laser spot size ($1/e^2$ radius) at 300, 450, and 600 K. (Filled and open markers denote measurements performed at UCR and UIUC, respectively.)

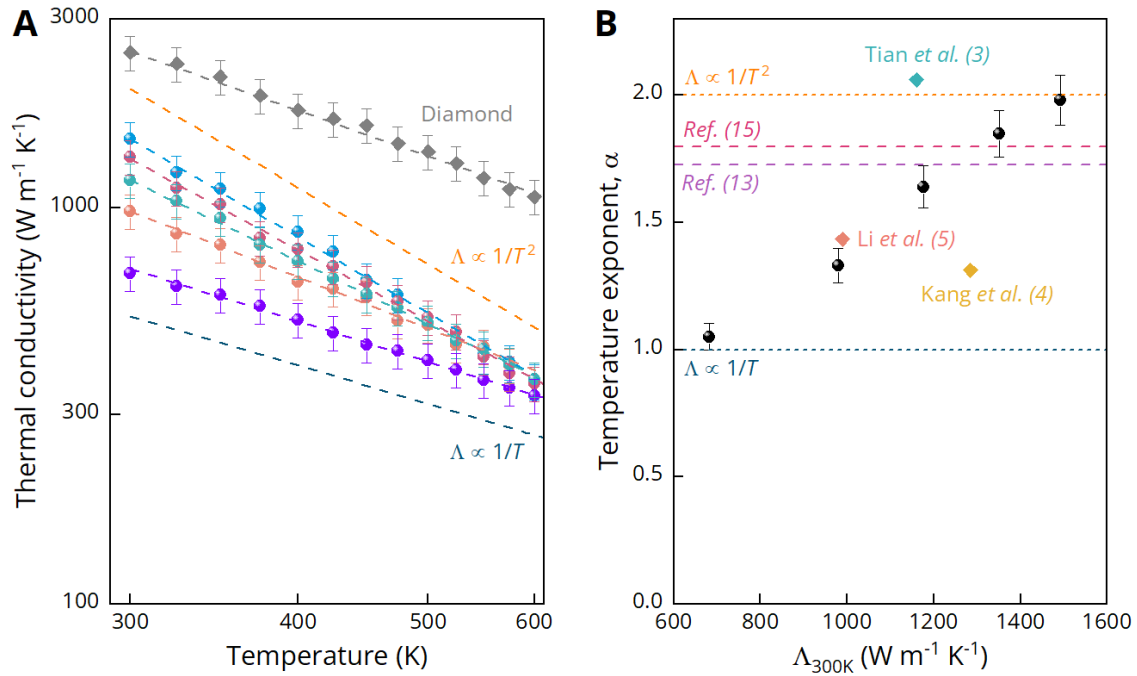


Fig. 2. Temperature-dependent thermal conductivity of five selected BAs samples. (A) Thermal conductivity of five selected BAs crystals and a type IIA diamond measured using TDTR. (B) The relationship between the temperature exponent and the room-temperature thermal conductivity of the five BAs crystals shown in (A). The temperature exponent α is obtained by fitting the thermal conductivity versus temperature data by $\Lambda \propto 1/T^\alpha$. Diamond markers are prior experimental results (3–5). Pink (15) and purple (13) dashed lines are theoretical predictions of α for isotopically pure BAs.

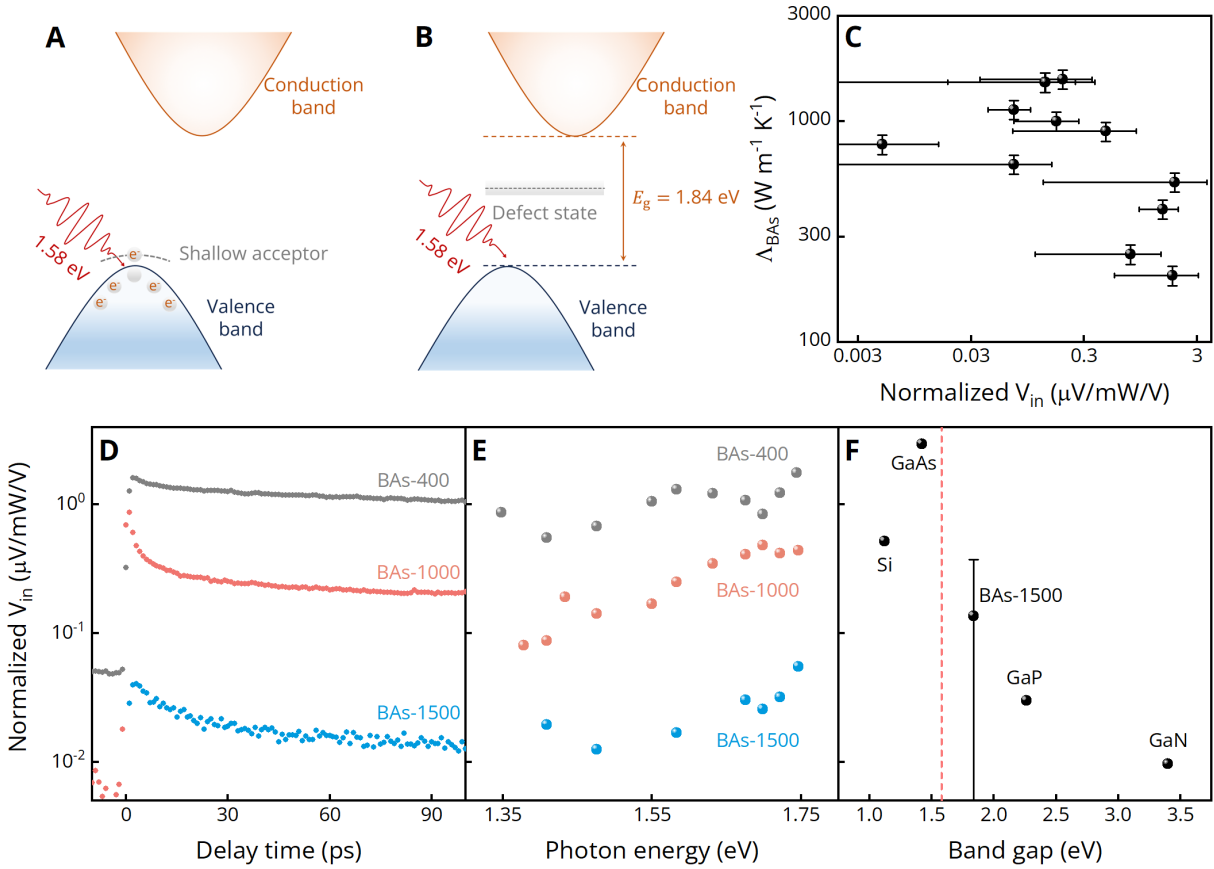


Fig. 3. Relationship between transient reflectivity microscopy signal and thermal conductivity of BAs. Free carriers from shallow donors/acceptors, and deeper defect states in the band gap cause optical absorption at photon energies below the band gap. Optical absorption of the pump beam leads to measurable transient reflectivity microscopy signal. (A) and (B) are schematics showing the impact of a shallow acceptor and a deep defect state on absorption of energies below the band gap, respectively. (C) Thermal conductivity of BAs crystals versus TRM signals obtained from bare BAs samples with 1.58 eV incident photons. The TRM signal was collected at a fixed delay time of 90 ps. Normalized V_{in} on the y-axis is the in-phase voltage measured by lock-in amplifier, normalized by the pump laser power and average voltage on the photodiode detector. (D) Time dependence of the transient reflectivity microscopy signal with 1.58 eV incident photons. (E) Transient reflectivity microscopy signals on three bare BAs samples as a function of excitation photon energy. (F) Transient reflectivity microscopy signals for bare Si, GaAs, BAs, GaP, and GaN single crystals. The vertical dashed line indicates laser energy.